Sodium-controlled interfacial resistive switching in thin film niobium oxide for neuromorphic applications

Journal:	*Chemistry of Materials*
Manuscript ID	cm-2024-00965w.R2
Manuscript Type:	Article
Date Submitted by the Author:	24-May-2024
Complete List of Authors:	Gaggio, Benedetta; University of Cambridge, Materials Science and Metallurgy Jan, Atif ; University of Cambridge, Department of Materials Science and Metallurgy Muller, Moritz; University of Cambridge Salonikidou, Barbara; University of Cambridge, Materials Science and Metallurgy Bakhit, Babak; University of Cambridge, Department of Engineering, Electrical Engineering Division; University of Cambridge, Materials Science and Metallurgy; Linkopings universitet, Department of Physics (IFM), Thin Film Physics Division Hellenbrand, Markus; University of Cambridge, Department of Materials Science and Metallurgy Di Martino, Giuliana; University of Cambridge, Department of Materials Science and Metallurgy Yildiz, Bilge; Massachusetts Institute of Technology, Departments of Nuclear Science and Engineering, and Materials Science and Engineering MacManus-Driscoll, Judith ; University of Cambridge, Dept. of Materials Science

Sodium-controlled interfacial resistive switching in thin film niobium oxide for neuromorphic applications

Benedetta Gaggio[1], Atif Jan[1], Moritz Muller[1], Barbara Salonikidou[1], Babak Bakhit[1,2,3], Markus Hellenbrand[1], Giuliana Di Martino[1], Bilge Yildiz[4,5], Judith L. MacManus-Driscoll[1]*

(1) Department of Materials Science and Metallurgy, University of Cambridge, 27 Charles Babbage Road, Cambridge, CB3 0FS, United Kingdom. (2) Electrical Engineering Division, Department of Engineering, University of Cambridge, JJ Thomson Avenue, Cambridge, CB3 0FA, United Kingdom. (3) Thin Film Physics Division, Department of Physics, Chemistry and Biology (IFM), Linköping University, Linköping SE-581 83, Sweden. (4) Department of Nuclear Science and Engineering, Massachusetts Institute of Technology, 77 Massachusetts Avenue, Cambridge, MA 02139, USA. (5) Department of Materials Science and Engineering, Massachusetts Institute of Technology, 77 Massachusetts Avenue, Cambridge, MA 02139, USA.

*Email: bg438@cam.ac.uk

Abstract: A double layer 2-terminal device is employed to show Na-controlled interfacial resistive switching and neuromorphic behaviour. The bilayer is based on interfacing

biocompatible $NaNbO_3$ and Nb_2O_5, which allows reversible uptake of Na^+ in the Nb_2O_5 layer. We demonstrate voltage-controlled interfacial barrier tuning via Na^+ transfer, enabling conductivity modulation and spike-amplitude and spike-timing dependent plasticity. The neuromorphic behaviour controlled by Na^+ ion dynamics in biocompatible materials shows potential for future low power sensing electronics and smart wearable with local processing.

Introduction: The rapid increase in demand for data-hungry technologies has led to a corresponding rise in the electricity usage of data centres[1,2]. As we reach the limits of device scaling (i.e., Moore's law), improvements in hardware efficiency beyond traditional von Neumann architecture become vital to enable data-hungry computation[3]. Taking inspiration from the synaptic modulations in the brain, memristive devices have attracted interest due to their ability to enable analog processing, where non-volatile resistive states are programmable via electrical bias[4–8]. Hardware efficiencies are also needed for the Internet of Things (IoT) devices, which are currently limited by the power consumption from continuous data storage and communication[9].

One type of emerging memristive technology is based on the resistive switching (RS) mechanism. Most RS technologies rely on redox changes, as the migration of ionic species controls the electronic conductivity of the metal oxide switching layer[10,11], with different functional materials having been explored for memristive applications[12–14]. In filamentary devices, charged species migration can form/rupture filaments that determine the resistance state[15,16]. However, when ionic migration occurs homogenously across the device, it may result in

gradual, controlled modulation of electronic barriers at thin film interfaces[17]. Interfacial switching mechanisms offer the potential advantage of better controllability, low stochasticity and high endurance[18–20] compared to filamentary switching. Often, oxygen vacancies are the ionic defects that are involved in both filamentary and interfacial switching[21,22]. Switching with small cations has also been studied, predominantly focusing on high mobility species like protons[23–25], or Li^+ ions [26,27].

Moreover, there have been promising reports employing interfacial control of Na^+ in TiO_2 with neuromorphic applications[28]. From a switching device perspective, Na^+ offers advantages over Li^+ and H^+ for conductance modulation, such as lower flammability than Li^+, and long term stability than Li^+ and H^+ due to its larger ionic radius[29]. In addition, from a biological perspective, Na+ is a common biomarker that plays a significant role in biological synapses, as neural networks operate by the motion of Na^+, K^+ and Ca^{2+} transport across membranes through interfacial processes[30–32].

Beyond traditional computing and CMOS-applications, neuromorphic computing is a critical component to achieve edge computing and reduce power consumption in IoT or smart wearables [19,33–36]. On top of reducing power consumption, edge computing has potential to reduce device complexity, remove wireless range and time latency limitations, and data privacy issues related to wireless data transfer[37]. The achievement of ionically controlled neuromorphic processing, where sensed ions are the active drivers of neuromorphic computation, enables response and

interpretation of environmental stimuli in a single integrated device, desirable for interfacing with biological systems[38,39].

T-Nb_2O_5 ('T' denotes the orthorhombic structure) is a widely studied anode material for energy storage applications due to its fast ion diffusion kinetics[40], as demonstrated in Li-[41–43] and Na-ion batteries[44,45]. Compared to other memristive materials, like TiO_2 and WO_3[23,29] that have been used in ionically driven RS switching, T-Nb_2O_5 offers distinct ionic transport properties that have not been explored for this purpose. Niobium oxides are employed in commercialized Li-ion batteries, showcasing the versatility of its channel structure for industrial, scalable use. Despite this, previous investigations of niobium oxides' memristive properties have mainly focused on oxygen vacancy filamentary[21,46–51], and threshold switching functionality[52–54], without demonstrating evidence for synaptic plasticity. There have been reports of Li^+ filamentary-based switching in $LiNbO_3$[55–57], but the neuromorphic properties or electrical robustness of these processes remain uncharacterized, despite reported intercalation dynamics of Li-ions[58,59].

We report neuromorphic performance based on interfacial switching modulated by the motion of Na^+ ions; specifically, the modulation of the interfacial Schottky barrier in a $NaNbO_3/Nb_2O_5$ solid-state 2-terminal device. Biological synaptic plasticity is shown for both spike-amplitude and spike-time dependent measurements, controlled by Na^+ dynamics. In this work, a $NaNbO_3$ layer is grown atop epitaxial Nb_2O_5 to serve as a source for Na^+. $NaNbO_3$ is a stable perovskite phase that has variable Na stoichiometry on the A site, which has been shown to accommodate at least 2% A-site deficiency[60]. Consequently, this is sufficient to dope the underlying Nb_2O_5 layer

by Na^+ reversibly as a function of bias. Both Na and O exchange is possible between the two layers, but we show via in-operando Raman methods that, thanks to the fast cation intercalation in T-Nb_2O_5, the Na^+ exchange dominates the conductivity modulation in the switching and neuromorphic behavior reported here. We show that the bilayer structure is critical to achieving non-volatile resistive states and synaptic plasticity functionality for neuromorphic applications. Furthermore, Nb_2O_5 thin films have been widely investigated in flexible electronics and biocompatible applications[34,61–63]. Na^+ switching enables synaptic learning ability in Nb_2O_5, offering new possibilities for smart sensing device applications.

Materials and Methods:

Fabrication: Nb_2O_5 targets are prepared by ball milling amorphous Nb_2O_5 powder (99.9% trace, Sigma-Aldrich, UK) in ethanol, pelletizing and sintering at 1073 K for 12 h. $NaNbO_3$ targets are prepared by ball milling amorphous Nb_2O_5 powder and Na_2CO_3 (99% trace, Sigma-Aldrich, UK) in ethanol in a 1:1 Nb:Na molar ratio, pelletizing and sintering at 1073 K for 12 h. Films were grown on conductive single-crystal Nb-doped strontium titanate (NbSTO) substrates in the (110) orientation by pulsed laser deposition (PLD) using a KrF excimer laser with a 248 nm wavelength. The deposition chamber is evacuated to sub 1 x 10^{-5} mbar, and the oxygen partial pressure during growth was kept constant at 1.3 x 10^{-2} mbar. The bilayer devices are grown without breaking vacuum. Both bilayer and single-layer devices are grown at 620 °C, with 0.9 mJ/cm^2 laser fluence, and shot frequency of 4 Hz. Single-layers devices are 50 nm in thickness; the total thickness of the bilayer device is also 50 nm, with 25 nm thick Nb_2O_5 and 25 nm thick

NaNbO3. For electrical characterisation, the films are patterned by UV lithography to obtain circular electrode pads of diameter 100, 50, 25 and 20 μm. Cr/Au (6/60 nm in thickness) top electrodes (TEs) are deposited by electron-beam evaporation, using a PVD 200 Pro (Kurt J. Lesker) instrument.

Materials characterisation: Cross-sectional transmission electron microscopy (TEM) analysis was performed on a FEI Tecnai Osiris microscope operated at 200 keV. Z-contrast images were acquired in scanning TEM high-angle-annular-dark-field (STEM-HAADF) mode. Energy-dispersive X-ray (EDX) elemental line scans were also obtained employing a FEI Super-X spectrometer embedded in the FEI instrument. The TEM specimen was prepared by focused ion beam (FIB) technique using a FEI Helios NanoLab microscope. The elemental compositions and depth profiles of the oxide thin films were obtained using time-of-flight elastic recoil detection analysis (ToF-ERDA), which is a powerful standard-free tool for quantitative analysis and depth-profiling with high accuracy, in particular, for light elements including Na and O. ToF-ERDA was carried out in a 5-MV 15SDH-2 tandem accelerator where recoils were detected in an angle of 45˚ with respect to the primary beam in a telescope measuring time-of-flight (ToF) using a foil-detector and energy in a gas ionization chamber in coincidence. This approach provides mass resolved data in ToF-vs-energy plots. Recoils were created by employing a 36-MeV $^{127}I^{8+}$ beam incident at 67.5˚ with respect to the surface normal of the samples. The depth profiles and average elemental compositions were determined from ToF-ERDA time-energy coincidence spectra using contes and Potku software packages. Raman spectroscopy was acquired through a thin TE Cr+Au (3+ 6 nm) layer that was deposited by thermal evaporation[64] using a 0.8-NA 100x

objective from Olympus, with integration times of 10 seconds. The Raman signals were excited using a 633 nm C.W. single-longitudinal-mode laser manufactured by Integrated Optics, and detected using a Kymera spectrometer that is connected to an Oxford Instruments Newton EMCCD camera. These measurements were collected on dedicated samples deposited on lanthanum aluminate (LAO) (110)/lanthanum strontium manganate (LSMO) (10 nm) substrate, of double thickness (50 nm Nb_2O_5 + 50 nm $NaNbO_3$), chosen to the strong Raman activity of NbSTO and improve film intensity.

Electrical characterisation: Current-voltage characteristics and spike measurements were investigated using a Keysight B2912A source measure unit and a probe station. Electrochemical impedance spectroscopy (EIS) is measured employing a Solartron impedance analyser, with frequencies ranging from 1 MHz to 1 Hz, and ac-voltage amplitude of 100 mV. In all electrical measurements, the bottom electrode (BE) is grounded, and the amplitude of read voltages is maintained at 0.1 V, including for ac-voltage EIS measurements.

Results and Discussion

We begin by presenting the structural and compositional information of $NaNbO_3$/Nb_2O_5 bilayer devices. We then show their electrical performance – IV scans, retention and endurance - and compare them with devices from the individual layers. Next, we explore the bilayer neuromorphic performance by studying spike-amplitude and spike-timing dependent plasticity.

In-situ Raman spectroscopy was employed to probe the critical role of Na^+ in the RS.

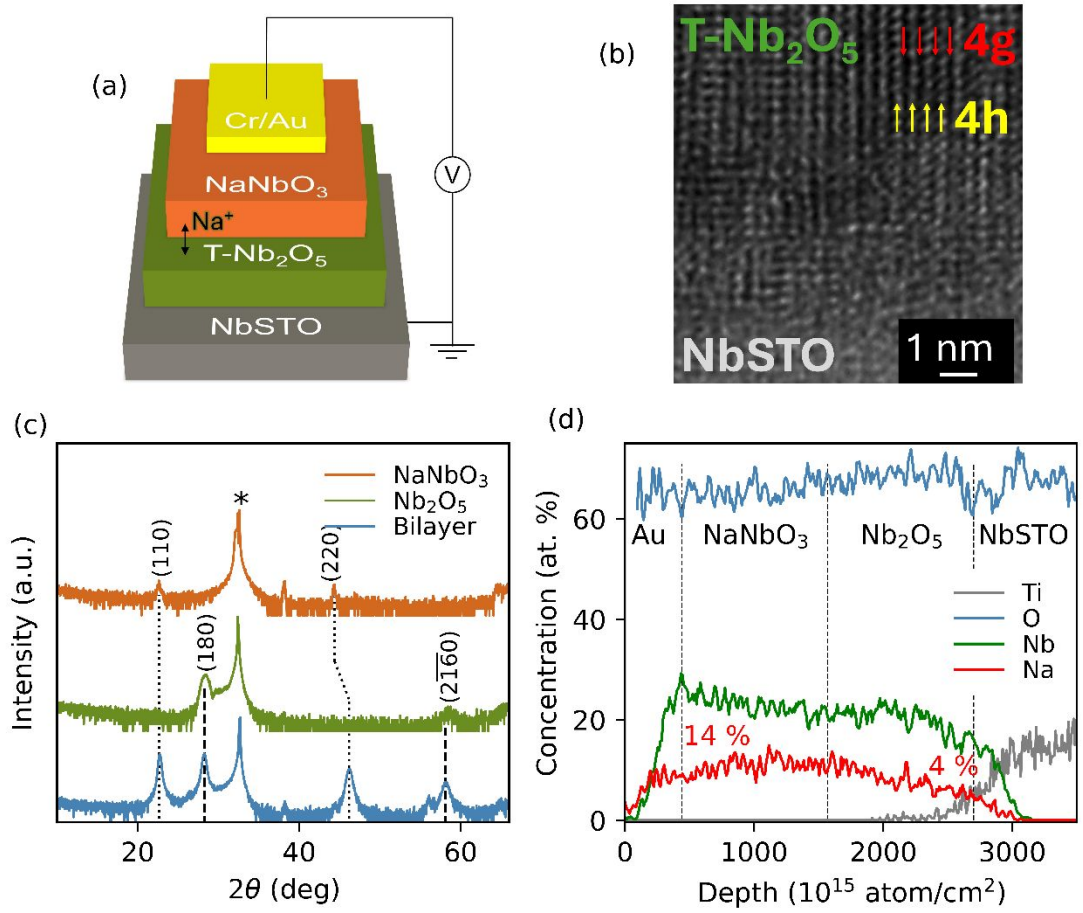

"**Figure 1.** (a) Schematic representation of bilayer structure used in this work: (110) NbSTO substrate/ T-Nb_2O_5/$NaNbO_3$/Cr/Au. (b) Cross-sectional HRTEM of device in (a), highlighting the alternating 4h (yellow) and 4g (red) layers in T-Nb_2O_5 that create atomic column-like structures. (c) XRD spectra of NbSTO/$NaNbO_3$ thin film (orange), NbSTO/T-Nb_2O_5 thin film (green), NbSTO/$NaNbO_3$/Nb_2O_5 bilayer (blue), dotted-lines highlight overlap of identified phase peaks for each individual layer, substrate peak signalled by asterisk. (d) ToF-ERDA depth profiling of bilayer device, with elemental quantification and analysis, showing Na-gradient forming across bilayer device."

Fig. 1(a) schematically illustrates the bilayer structure of the NbSTO/Nb_2O_5/$NaNbO_3$/Cr/Au stack. Fig. 1(b) shows the cross-sectional HRTEM image of the T-Nb_2O_5 film with a dense nanostructure epitaxially grown on 110-oriented NbSTO. This nanostructure consists of alternating densely and loosely packed Nb-oxide polyhedral sheets (4h and 4g, respectively). Griffith et al. showed that the layered nanostructure in epitaxial T-Nb_2O_5 enables fast cation migration through atomic column-like structure of low steric hindrance (low Nb-density)[41]. It was already reported that a (110) perovskite substrate is critical to achieve the perpendicular orientation of the 4h/4g columns with respect to the T-Nb_2O_5 plane[58].

Fig. 1(c) compares the XRD spectra of the bilayer (blue) to those of its constituent single layers, Nb_2O_5 (green) and $NaNbO_3$ (orange). The diffraction peaks appeared at $2\theta = 28.40^\circ$ and 58.78° are attributed to the (180) and ($2\underline{16}0$) orientations of the large orthorhombic cell of Nb_2O_5 (T-phase, a = 6.175 A, b = 29.175 A, c = 3.920 A; $\alpha = \beta = \gamma = 90^\circ$), as previously reported[65]. $NaNbO_3$, deposited on top of T- Nb_2O_5, is in its orthorhombic phase (Pmc2, a = 5.53, b = 5.61, c = 7.79 A; $\alpha = \beta = \gamma = 90^\circ$), as determined by the XRD peaks at $2\theta = 22.42^\circ$ and 44.12°, attributed to (110) and (220) reflections in both the single layer (orange) and bilayer film (blue). The growth temperature is optimized to 620° C to achieve the columnar structure of T-Nb_2O_5. This is below the ideal growth temperature for epitaxial $NaNbO_3$ and so it results in a polycrystalline layer as evidenced from XRD.

A ToF-ERDA elemental depth profile of the pristine NbSTO/Nb_2O_5/$NaNbO_3$/Cr/Au stack is given in Fig. 1(d). Both Nb and O have an almost uniform distribution along the Nb_2O_5/$NaNbO_3$ bilayer. While Na is uniformly distributed along the thickness of the $NaNbO_3$ top layer (with an average concentration of 14 at. %), it has a gradient in the Nb_2O_5 bottom layer; significantly decreasing from 14 at. % (the Nb_2O_5/$NaNbO_3$ interface) to 4 at. % (the NbSTO/Nb_2O_5 interface). This indicates the high diffusivity of Na in the Nb-based oxides that can provide versatile cation mobility upon applying bias, which is essential for low-power RS. To show the challenge of Na-doping the Nb_2O_5 layer in PLD, 5 films deposited from targets of varying Na:Nb ratios (1, 0.8, 0.5, 0.2) are compared (XRD, Supplementary Fig. S2). It is found that only targets closest to the $NaNbO_3$ precise stoichiometric ratio led to the observation of $NaNbO_3$-related peaks. To confirm the greater stability of stoichiometric $NaNbO_3$ versus Na-deficient $NaNbO_3$, ToF-ERDA analysis was further performed on these samples (Supplementary Fig. S2). The presence of Na is only observed for the stoichiometric case. As already mentioned, the stability of the top cation source is critical to its choice as a controlled Na source for the doping of the Nb_2O_5 host.

The device was contacted via a Cr/Au TE, achieving a 2-terminal configuration, ideal for its simplicity[66]. Since the electrical bias is applied parallel to the T-Nb_2O_5 channels, this creates a source/host structure for the charge carrier species to exchange under the bias application at the TE, and grounding at the BE, NbSTO. Fig. 2(a) shows the characteristic RS counterclockwise pinched-loop, showing set/reset transitions at ±2 V, which switch the device between low resistive state (LRS) and high resistive state (HRS) in a bipolar fashion. The switching process is forming-free and gradual, ideal features for an analog artificial synapses candidates[67]. The

current is found to be linearly proportional to electrode pad size (10, 12.5, 25 and 50 um radii, Fig. 2(a) inset), which is evidence for interfacial switching and not a filamentary-dominated mechanism, and this is in agreement with previous results reported for Schottky barrier devices[18]. On the contrary, filamentary Nb_2O_5 switching devices show abrupt jumps in current and filament formation/rupture events[51], which limit the uniformity from cycle to cycle and across devices. Uniformity is a crucial requirement RRAM-based synaptic devices, affecting training accuracy, power consumption and overall performance efficiency of the device at large-scale. Here, we focus on cycle-to-cycle uniformity on a single device batch (Supplementary Fig. 3), however, to bring this material and device structure closer to application, future work should investigate uniformity across batch depositions, employing practical fabrication methods that enable large-area deposition (see conclusion for further discussion on PLD and other fabrication methods for niobium oxides).

To assess the retention performance, the device is set with a pulse of 2 V (and reset with -2 V) for 1 s, and the resulting resistance states are read with a pulse of 0.1 V (Fig. 1(b)) for 1000 pulses at 1 s intervals. The positive pulse sets the device into the LRS, which increases by 12% of its initial resistance in the first 1000 s, followed by a plateau. The LRS is conserved after 24 h, with a further 4% increase. The negative pulse resets the device to the HRS, stable within 6% of its initial state for the first 1000 s, and stable after 24 h. In Supplementary Fig. 3, we compare the retention for bilayer and single layer devices: notably, non-volatile behavior is observed only for the bilayer, whilst the single layers decay back to their initial state. Importantly, using the $NaNbO_3$ as Na-doping source in combination with the ion conducing Nb_2O_5 is critical for

achieving the non-volatile RS performance studied herein. Hence, the interfacing of a stable Na-source with Nb_2O_5 enables conductance tuning as a response to applied field, showing sensing behavior of the device stack. The integrated ionic monitoring and memristive functionality can have interesting applications towards sensing edge computing usage cases, such as biocompatible monitoring. It is noteworthy that the ionic exchange between Nb_2O_5 and $NaNbO_3$ could be expected to involve both Na^+ and oxygen species under the same bias polarity, however, we suggest that, thanks to the faster mobility of Na-cations in T-Nb_2O_5, the Na^+ exchange dominates the conductivity modulation. We further employ in-operando Raman and temperature-dependent measurements to show Na-specific chemical composition modulations.

The device endurance is demonstrated in Fig. 2(c), by applying $\pm$ 2 V write pulses of 25 ms duration and 0.1 V reading pulses. The device shows uniform and reliable cyclability across >8000 cycles, maintaining a stable memory window and IV sweep response (Supplementary Fig. S3). The retention and endurance performances are fit for both short- and long-term learning operations[68]. The memory window is tunable depending on amplitude and time of pulse train, as demonstrated further in the neuromorphic characterisation section. This functionality can be applied towards translating stimuli sensing to a resistance state. The conductance modulation shows promise towards multilevel-state performance, which is out of scope of this investigation, but is promising behavior for ultra-low power neuromorphic and biosensing applications. The on/off ratio maximum is found to be 3.6 (Supplementary Fig. S4), lower than generally reported values[33] but compliant with neuromorphic operation requirements[69,70]. It is noteworthy to mention that Nb metal oxide systems with Li^+ ion intercalation have been reported with large conductance

changes, based on a different mechanism: the oxide undergoes an insulator-to-metal transition (IMT) due to the formation of the $LiNbO_3$ phase and population of the Nb-centre conduction band[58]. Also, previous reports have shown analogue behavior in Nb_2O_5 controlled by an electronic charge trapping mechanism, however the behavior is limited by poor retention[71]. On the contrary, the non-volatile analogue and interfacial switching nature of the bilayer device reported with strong electronic robustness enables neuromorphic and sensing applications, as we further explore in the next section.

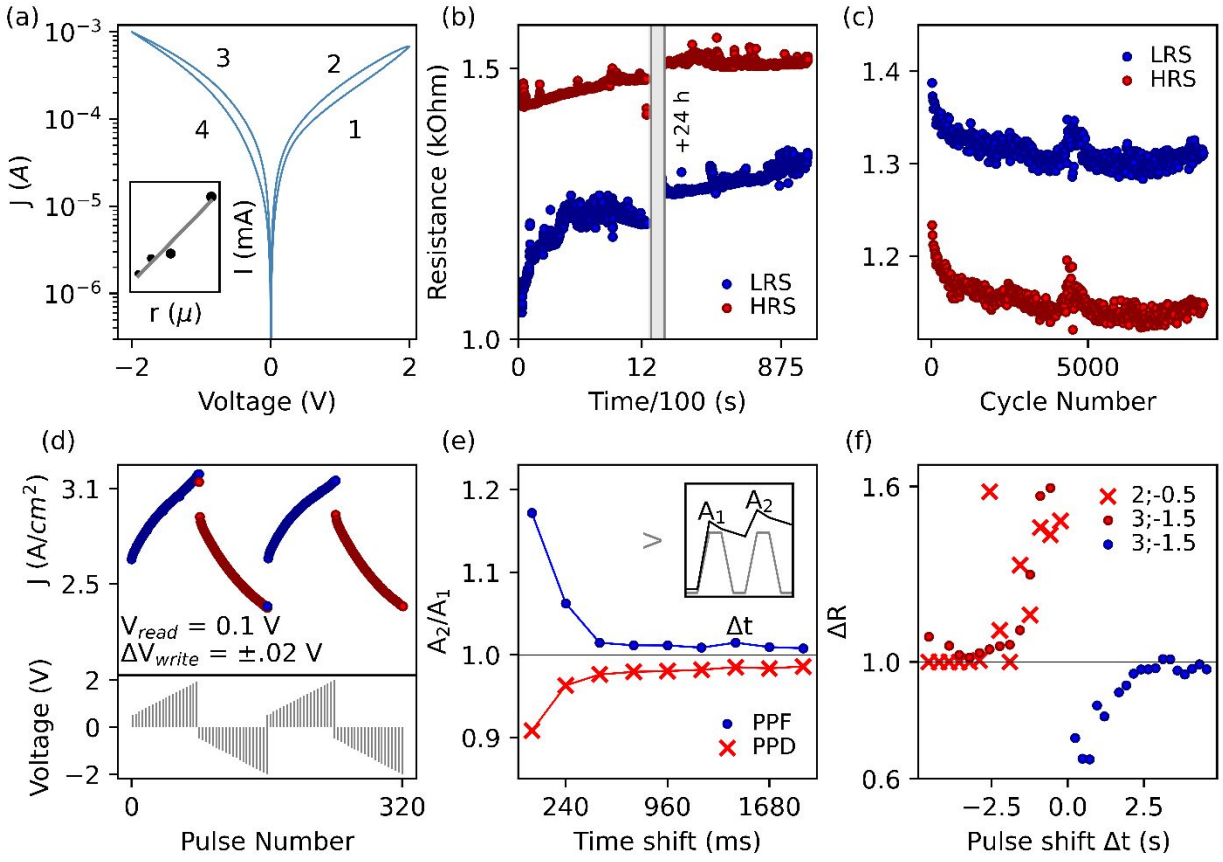

"**Figure 2.** (a) I-V characteristics of bilayer device with CCW direction of RS; inset presents area-dependent current. (b) Retention plots for bilayer device showing non-volatile HRS/LRS

after ±2V set/reset pulses (red and blue, respectively) read at 0.1 V per second for 1000 s, the measurement is then repeated for LRS and HRS on the same respective devices after 24 h. (c) Endurance plots for 8000 RS cycles on bilayer device after ±2V set/rest pulses, read at 0.1 V. (d) Potentiation and depression of device synaptic weight via increasing train pulses from 0.5 to 2, in $\Delta V = \pm 0.1$ V with 0.1 V pulse read, inset showing schematic of voltage profile. (e) (PPF, red) and depression (blue) using two consecutive +2 V and -2 V pulses, respectively, showing A2/A1 index ratio as a function of pulse interval time. (f) Asymmetric STDP demonstrating learning ability in device resistance potentiation and depression as a function of pre and post synaptic voltage pulse interval time."

Neuromorphic devices with sensory functions have the capacity to process information from the perceived surroundings at ultralow power by emulating neural learning functionality[33,72]. On top of ionic sensitivity, materials for neuromorphic applications must therefore be able to satisfy some key functionalities. Synaptic plasticity is the ability of a synapse to modulate its weight, which in turn determines the efficiency with which adjacent neurons are able to propagate information amongst each other, represented here as the device resistance[73]. Plasticity can be differentiated into long-term and short-term (LTP and STP, respectively). LTP denotes a non-volatile state equivalent, and in other words underpins the formation of long-term memory in learning functions – hours to years. STP refers to temporary functions in shorter time windows - milliseconds to minutes - to enable tasks such as various stimuli recognition, filtering and perception[74]. In the peripheral nervous system, for example, STP functionality enables stimuli

detection and information processing on different sites without relying on relaying information to the central nervous system. In analog sensor devices, STP can be employed to perform brain-inspired algorithms where recent neural activity has to be tracked[37]. In the brain, the action potential has been found to have five orders of complexity, i.e. state variable dependencies that determine the electrical spike profile taking place across neurons and synapse[75,76].

Fig. 2(d) shows spike amplitude-dependent plasticity (SADP), investigated by application of a train of pulses of increasing voltage, from 0.5 to 2 V (and -0.5 to -2 V), with $\Delta V = \pm 0.1$ V, and each pulse followed by a 0.1 V read pulse (Fig. 2(d), bottom inset). The device resistance is tuned by the amplitude of the write pulse, showing alternating potentiation and depression of the resistance state, where each data point represents the average read-out after each pulse has been applied. This effect is analogous to synaptic weight plasticity, and is found to be reversible, resilient to cyclability and uniform across different devices tested (Supplementary Fig. S5). We demonstrated 80 states each per potentiation and depression, with an average percentage change in resistance of 0.20% and -0.27%, respectively. These values are in line with similar ionic systems, such as protonic conductance changes in WO_3 systems[23].

Next, we investigate the role of spike-timing in the modulation of synaptic weights (Fig. 2(e-f)). Firstly, STP learning behavior is investigated by performing paired-pulse facilitation (PPF): two consecutive pulses are applied to the bilayer, alternating potentiation (+1 V) and depression (-1 V), at increasing time shifts (from 240 ms to 2 s) (Fig. 2(e)). The ratio between the amplitudes of the two current peaks, defined as postsynaptic spikes A1 and A2, is then plotted as a function of

pulse interval[74]. In agreement with the STP behavior observed in short-term memory and neural networks mechanics, the post-synaptic ratio is dependent on the pulse time interval, showing a greater change for closely timed pulses. The frequency dependence observed in neuromorphic devices has been previously related to intrinsic switching mechanism time constants: when the pulse pair interval is shorter than the mechanism relaxation dynamics, the non-equilibrium states are stimulated by the second pulse and the change in conductance effect is maximized.

Secondly, we investigated the modulation of synaptic weight as well as direction (potentiation or depression), by the temporal order, or time shift, between pre and postsynaptic spike. Pre- and post-synaptic pulses are simulated at time intervals (from 240 ms to 5 s) and summed so that the overall voltage is applied at the TE; the pulses are asymmetric (Supplementary Fig. S6). By negative time interval, we denote the pulse in the order pre → post-synaptic, and positive as pulses being post → pre-synaptic. Each response is measured after applying a set (or reset) pulse of constant amplitude to bring the device back into its LRS (HRS). In Fig. 2(f), the bilayer changes in resistance, $|\Delta R|$, as a function of time intervals, indicating an inverse proportionality to time shift. This behavior has been previously associated to asymmetric Hebbian learning and has potential for applications in spiking neural networks systems, where frequency of a train of pulses is converted into a response of proportional intensity[77]. In both time-dependent measurements, PPF and STDP, the time intervals investigated for synaptic weight modulation are approximately one order of magnitude slower than biological stimescales[78,79]. However, this limitation is introduced by the experimental set up rather than the actual devices, thus still

showing promising use of Na^+ ion dynamics in biocompatible electronics. Switching speed is a meaningful parameter when evaluating the performance of devices for artificial neural networks (ANNs) applications, as it enhances fast training and operational efficiency. The scope of this work is to report on successful control of synaptic plasticity in Na-doped systems. However, future work should further explore how to translate the fast-charging performance of columnar structure of T-Nb_2O_5 in energy storage applications to RS speed for neuromorphic devices.

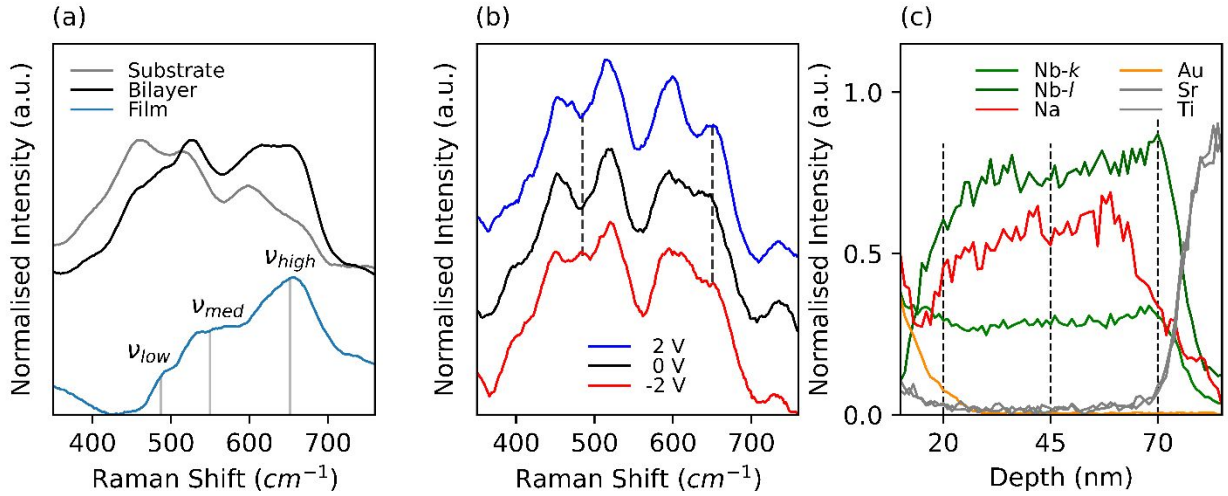

"**Figure 3.** (a). Raman spectroscopy measurement for LAO/LSMO substrate (grey) and LAO/LSMO/ Nb_2O_5/$NaNbO_3$ bilayer device (black), the active film Nb_2O_5/$NaNbO_3$ spectra (blue) is obtained by subtraction of the substrate spectra. (b) In-operando Raman measurements of bilayer device, showing changes between pristine bilayer spectra (black) and after bias application: LRS after +2 V pulse (blue) and HRS after -2 V pulse (red). (c) EDX measurements on a cross-sectional sample measured by STEM (HAADF) in its LRS, showing Na-signal accumulation towards the Nb_2O_5/NbSTO interface."

The modulation of interfacial energy barriers in the bilayer device was further probed by in operando Raman to show the voltage-dependent migration of Na^+ cations in the device. A bilayer film was grown on a LAO substrate with a 8 nm LSMO layer as conductive back contact, as the NbSTO substrate (employed in the default bilayer devices described in the rest of the paper) is highly Raman active, and obscures the film signal. The Raman plot of the full bilayer stack is shown in Fig. 3(a); the strong peak around 600 cm^{-1} is attributed to the LAO/LSMO signal[80]. To further isolate the Nb_2O_5/$NaNbO_3$ active layer contribution, the Raman signal of the bare substrate LAO/LSMO (Fig. 3(a), grey) is subtracted from the full bilayer stack (LAO/LSMO/Nb_2O_5/$NaNbO_3$) signal (Fig. 3(a), black. The Nb_2O_5/$NaNbO_3$ Raman spectra (Fig. 3(a), blue) shows a prominent peak ν_{high}~ 655 cm^{-1}, accompanied by a shoulder ν_{med}~ 540-560 cm^{-1}, and a smaller shoulder ν_{low}~ 460-490 cm^{-1}. The results closely correspond to the $NaNbO_3$ literature, attributing the high shift ν_{high} and medium shift ν_{med} regions to the NbO_6 octahedra symmetric and asymmetric stretches in $ANbO_3$ (A = Li, Na, K) compounds, while low shift region ν_{low} is associated to O-Nb-O bending modes in $ANbO_3$ compounds[81,82].

Fig. 3(b) shows the in-operando characterisation of the LAO/LSMO/$NaNbO_3$/Nb_2O_5 device, wherein Raman spectra were acquired concurrently under bias switching between ±2 V. The signal from LAO/LSMO is not subtracted here as it is expected to have bias-dependencies. The in-operando measurement enabled the study of the immediate effect of the applied bias on Na-intercalation and changes in the device chemical. Fig. 3(b) reveals the changes in Raman spectrum shape and intensity between the pristine state, HRS (red) and LRS (blue). At +2 V (Na^+

ions move away from TE), a rise in peak intensity is observed in the high wavenumber region at 655 cm^{-1}, compared to the pristine state (at 0 V), while at -2 V (Na^+ ions move towards TE), the intensity of this peak is reduced. The low wavenumber region, 450-490 cm^{-1} is also voltage-dependent, showing increased signal intensity upon -2 V pulse application. Chen et al. have previously investigated the correlation between T-Nb_2O_5 Raman spectra and cation intercalation. The group showed that, upon deintercalation, the high wavenumber peaks increase due to reduced coordination between oxygen and cation species and enhanced stretching modes observed[40]. Moreover, the low wavenumber peaks representing the bending vibration are expected to decrease due to the compression of NbO_x polyhedral from A-site vacancies in $ANbO_3$[60]. Therefore, in-operando Raman results observed in the bilayer device closely match the Na-intercalation effects previously reported in the literature, confirming that the applied bias drives the cation (de)intercalation in the device, across the Nb_2O_5 and $NaNbO_3$ layers.

To investigate this phenomenon further, the in-operando measurements were repeated on the undoped Nb_2O_5 single layer device, where oxygen vacancies could be expected to accumulate at interfaces in response to the applied bias. Supplementary Fig. S7 shows that no change is observed in the high shift region at 655 cm^{-1}, which allows us to attribute the changes observed in Fig. 3(b) to voltage-controlled Na^+ migration. In fact, it is well known that small cations benefit from low steric hindrance in the T-Nb_2O_5 channeled layer, and so fast ionic migration, which we further address in the next section via temperature-dependent measurements. Moreover, the polarity of potential applied was reversed (Supplementary Fig. S7) and the

opposite trends compared to Figure 3(b) were observed, verifying the reliability of the measurement.

Cross-sectional scanning transmission electron microscopy (STEM) bright-field images of the bilayer device are presented in Fig. 3(c). The chemical composition of the cross-section was investigated by energy dispersive X-ray (EDX) spectroscopy. More precisely, a device previously set to its LRS was investigated ex situ to study the non-volatile distribution of the Na^+ ions. We observe a Na-species gradient which increases by 25% from $NaNbO_3$ to Nb_2O_5 with a higher concentration found at the Nb_2O_5/NbSTO interface. Thus, the measurement confirms that setting the device via a positive pulse leads to the non-volatile accumulation of the Na-species away from the TE. In comparison, the ToF-ERDA depth profile presented in Fig 1(d) shows that,

in a pristine HRS device, the Na-species gradient *decreases* from $NaNbO_3$ to Nb_2O_5.

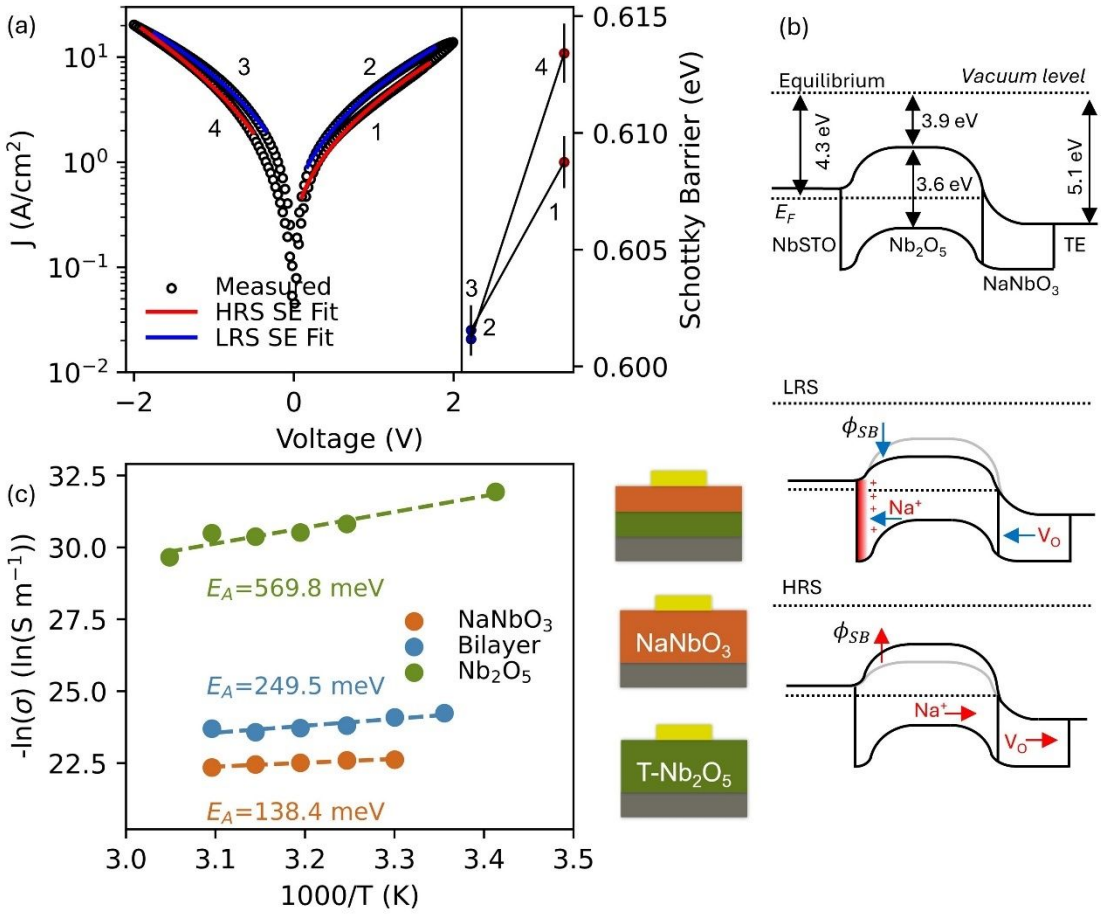

"**Figure 4.** (a). Left: Schottky emission fit over measured IV sweep data; right: Schottky barrier modulation upon set and reset voltage pulse operations. (b) From top to bottom: band diagram model for equilibrium, LRS and HRS. (c). Left: Arrhenius derived conductivities versus $\frac{1}{T}$ showing activation energies for bilayer device (blue), Nb2O5 (green) and NaNbO3 (orange) individual layer devices; right schematic cross-sectional models for systems studied in temperature-dependent derivation."

Fig. 4(a) shows a representative IV curve, fitted with a Schottky emission mechanism that provides a consistently low error fit across the mid-voltage range of the IV scan (i.e. 0.2 to 2.0 V), suggesting that it represents the dominating mechanism at play. The Schottky barrier (SB) is extracted according to (Eq. 1):

$$J = A^{*}T^{2}\exp\left[\frac{-q}{k_B T}\left(\Phi_B - \sqrt{\frac{qE}{4\pi\varepsilon_0\varepsilon_{op}}}\right)\right]$$

Where J is current density (A/cm^2), $A^{*} = \lambda A_0$is the effective Richardson constant, taken to be $A_0 = 1.2 \times 10^{6}$ (A/m^{2}T^2) and $\lambda = 0.5$, $T = 291$ is temperature (Kelvin), ε_0 is the permittivity of vacuum, Φ_B is Schottky barrier (eV), ε_{op} is the optical dielectric constant, both to be calculated. Fig.4(b) compares the SB at various points of the IV curve, to show the quantitative change, ΔSB, found to be ±0.015 across set/reset. We note that similar changes in SB were reported for an interfacial Na-based system in 2-terminal Na-doped TiO_2 devices, where Na-ions are the main switching charge carrier[28]. We suggest that, because of the large doping present in the Nb_2O_5 layer, the Na-cation gradient formed at the interfaces after electrical pulsing is limited, leading to smaller SB changes and overall smaller on/off ratios observed. However, neuromorphic functionality is still shown, and in small amplitude ranges, compatible with sensing applications[68].

A temperature-dependent fit of thermionic emission[83] was then performed to sustain the voltage-dependent derivation presented above of the Schottky mechanism (Supplementary note 8). The

Richardson plot derivation of the SB shows good agreement to the voltage-dependent method described above, consolidating the suitability of Schottky emission as the dominating conduction mechanism to describe the behavior observed.

We can understand the resistive switching and neuromorphic behavior shown in Fig. 2(a-f) based on the homogenous infiltration of sodium in the Nb_2O_5 thin film (Fig. 1(b-c)) and its voltage control (Fig. 3(a-c)). In the 2-terminal device configuration, the column-like structure of the T-Nb_2O_5 lies perpendicular to the plane, and parallel to the applied bias, enabling voltage-controlled migration of Na-species. IV (Supplementary Fig. S4) and EIS measurements (Supplementary Fig. S9) show that the as-grown $NaNbO_3$ layer (R: 200 Ohm) is more conductive than the Nb_2O_5 single layer (R_{HRS}: 1.5e3 Ohm) and the Nb_2O_5/$NaNbO_3$ bilayer device (R: 8.2e7 Ohm). Thus, the Nb_2O_5 is the active switching layer, whereas the $NaNbO_3$ is passive to the switching but is critical as a stable Na-source. For consistency, we therefore only use the Nb_2O_5 thickness in the calculations of the electric field presented here and refer to the $NaNbO_3$/TE interface as Ohmic.

In the positive voltage sweep, applied at the TE, the Na^+ species accumulate at the NbSTO/Nb_2O_5 interface, which is the dominating conduction barrier in the case of a positive voltage at the TE. As the Na dopants act as electron donors due to the low ionization energy, the increase in Na-concentration at the interface reduces the Schottky barrier height, which sets the device to the LRS. With the application of the negative sweep at the TE, the Na^+ ions move away from the Nb_2O_5/NbSTO interface, resetting the device to a HRS for the following positive

voltage sweep. As mentioned earlier, it is possible that oxygen species also exchange across the Nb_2O_5/$NaNbO_3$ interface: in a negative sweep, oxygen vacancies accumulating in the $NaNbO_3$ would reduce the Schottky barrier at the Nb_2O_5/$NaNbO_3$, which is the dominating conduction barrier for a negative voltage at the TE. Importantly, different from the IV sweeps, where the two Schottky barriers limit the current for positive and negative voltages at the TE, in the endurance/retention and neuromorphic measurements of Fig. 2(a-f), the read pulses are positive, so that the Schottky barrier at the Nb_2O_5/NbSTO interface is the limiting barrier for both the HRS and LRS. Oxygen-vacancies have also been shown to enhance the Li-ion intercalation process[84] in T-Nb_2O_5 systems.

Finally, the temperature-dependent ionic diffusion activation energy of the bilayer is compared to those of its constituent layers, more precisely the Nb_2O_5 and $NaNbO_3$ single layers. For each device, the EIS spectra are measured over a temperature range and fitted by an equivalent circuit (Supplementary Note 10). The activation energy of diffusion (Fig. 4(c)) is then derived from (Eq. 2):

$$\sigma = A \times e^{\frac{-E_A}{k_B T}}$$

Where σ is conductivity (S/cm), A is pre-exponential factor, k_B is Boltzmann constant, T is temperature (Kelvin) and E_A is the activation energy to conduction (eV). Firstly, for the bilayer we report an activation energy of 249.5 meV, in excellent agreement with literature Na-cation diffusion values in metal oxides, and small cation diffusion reported for T-Nb_2O_5 systems studied previously[85–88]. In comparison, the largest activation energy is obtained for the pristine Nb_2O_5

device, 569.8 meV. This value is in excellent agreement with previously reported oxygen vacancy activation energy, in Nb_2O_5 thin films[89–91], which do not travel via the columnar-structure and are hence not kinetically facilitated by the orthorhombic phase. The values obtained indicate that the Na^+ ion is the dominating charge carrier, responsible for the interfacial switching in the bilayer device, as presented by our mechanism model.

Conclusion

In conclusion, a double layer $NaNbO_3/Nb_2O_5$ is studied to show the Na^+ control of interfacial RS. The interfacing of these two layers enables uniform Na-doping, leading to voltage-controlled migration of Na^+ species in the Nb_2O_5 layer, facilitated by perpendicularly grown columnar structures. Electrical characterisation highlights formation-free and gradual RS, indicative of interfacial mechanisms, with robust retention. The device shows synaptic weight modulation by both spike-time and amplitude dependencies, characterised by SADP and STDP studies. In operando Raman spectroscopy elucidates the voltage-dependent migration of Na^+ within the device, supporting a Na^+ modulated conductivity. Additionally, EDX spectroscopy confirms the non-volatile distribution of Na^+ species in the device LRS configuration. We propose a Schottky emission mechanism, controlled by Na^+ dynamics as primary charge carrier at the conduction barrier interfaces, driving the device between LRS and HRS under positive and negative voltage sweeps, respectively.

Whilst PLD enables epitaxial thin film growth with high stoichiometric control, it does not translate to industry. Future work will explore the translation of this system to more practical

fabrication to enable larger area, necessary for high-density crossbar array application. Nb_2O_5 thin film growth by sputtering or atomic layer deposition (ALD) on silicon is well-established for electronics applications, and the orthorhombic phase, critical for ionic intercalation purposes, has also been scaled up for the commercialisation of Nb-based Li-ion batteries. However, the translation of the vertically oriented nanocolumns in T-Nb_2O_5 from single crystal substrates (i.e., NbSTO, LAO) to more practical substrates has not been yet explored.

Supporting Information: Details of thin film surface morphology and composition studies; characterisation of device uniformity in electrical and neuromorphic measurements; comparison of Na-doped and undoped sample performance; further electrical, in-operando material and impedance characterisation detail; derivation of Schottky barrier.

Acknowledgments: BG gratefully acknowledges the Wolfson EM Suite from the University of Cambridge Materials Science and Metallurgy Department, SG, CD and JW for their mastery and guidance in FIB, HRTEM and STEM measurements. BG and MM thank the EPSRC CDT MRes/PhD Studentship in Nanoscience and Nanotechnology (NanoDTC Cambridge EP/S022953/1) grant for funding their PhD scholarship. JLM-D thanks the Royal Academy of Engineering Chair in Emerging Technologies grant, CIET1819\24. JLM-D, BS, and MH thank the ERC grant EU-H2020-ERC-ADG#882929 EROS. BY gratefully acknowledges the Leverhulme Trust for supporting her Visiting Professorship at University of Cambridge. GDM and AJ acknowledge support from Royal Society (grant RGS\R1\221262), EPSRC

(EP/X034593/1 and Winton Programme for the Physics of Sustainability; selected by the ERC, funded by UKRI). BB gratefully acknowledges financial support from Swedish Research Council (VR), grant 2019-00191 (for accelerator-based ion-technological centre in tandem accelerator laboratory in Uppsala University, Sweden) and grant 2021-00357, the University of Cambridge's "Knowledge Exchange and Impact award", CAPE BlueSky Research Award 2022, Energy IRC Small Grant award for Knowledge Exchange and Impact from the Higher Education Innovation Fund (HEIF), and Cambridge Royce facilities grant EP/P024947/1 and Sir Henry Royce Institute - recurrent grant EP/R00661X/1.

TOC Graphic:

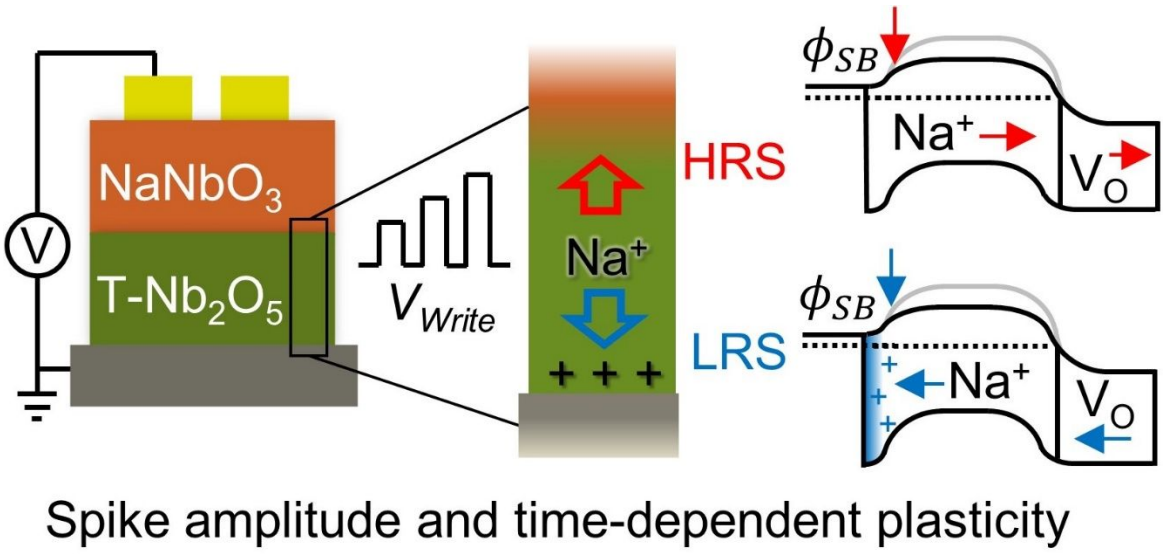

References

(1) Gupta, U.; Kim, Y. G.; Lee, S.; Tse, J.; Lee, H.-H. S.; Wei, G.-Y.; Brooks, D.; Wu, C.-J. Chasing Carbon: The Elusive Environmental Footprint of Computing. *IEEE Micro* **2022**, *42* (4), 37–47. https://doi.org/10.1109/MM.2022.3163226.

(2) Jones, N. How to Stop Data Centres from Gobbling up the World's Electricity. *Nature* **2018**, *561* (7722), 163–166. https://doi.org/10.1038/d41586-018-06610-y.

(3) Salahuddin, S.; Ni, K.; Datta, S. The Era of Hyper-Scaling in Electronics. *Nat. Electron.* **2018**, *1* (8), 442–450. https://doi.org/10.1038/s41928-018-0117-x.

(4) Park, T. J.; Deng, S.; Manna, S.; Islam, A. N. M. N.; Yu, H.; Yuan, Y.; Fong, D. D.; Chubykin, A. A.; Sengupta, A.; Sankaranarayanan, S. K. R. S.; Ramanathan, S. Complex Oxides for Brain-Inspired Computing: A Review. *Adv. Mater.* **2023**, *35* (37), 2203352. https://doi.org/10.1002/adma.202203352.

(5) Schenk, T.; Pešić, M.; Slesazeck, S.; Schroeder, U.; Mikolajick, T. Memory Technology-a Primer for Material Scientists. *Rep. Prog. Phys. Phys. Soc. G. B.* **2020**, *83* (8), 086501. https://doi.org/10.1088/1361-6633/ab8f86.

(6) Tang, J.; Yuan, F.; Shen, X.; Wang, Z.; Rao, M.; He, Y.; Sun, Y.; Li, X.; Zhang, W.; Li, Y.; Gao, B.; Qian, H.; Bi, G.; Song, S.; Yang, J. J.; Wu, H. Bridging Biological and Artificial Neural Networks with Emerging Neuromorphic Devices: Fundamentals, Progress, and Challenges. *Adv. Mater.* **2019**, *31* (49), 1902761. https://doi.org/10.1002/adma.201902761.

(7) Banerjee, W.; Nikam, R. D.; Hwang, H. Prospect and Challenges of Analog Switching for Neuromorphic Hardware. *Appl. Phys. Lett.* **2022**, *120* (6), 060501. https://doi.org/10.1063/5.0073528.

(8) Yoon, J. H.; Song, Y.-W.; Ham, W.; Park, J.-M.; Kwon, J.-Y. A Review on Device Requirements of Resistive Random Access Memory (RRAM)-Based Neuromorphic Computing. *APL Mater.* **2023**, *11* (9), 090701. https://doi.org/10.1063/5.0149393.

(9) Caiazza, C.; Giordano, S.; Luconi, V.; Vecchio, A. Edge Computing vs Centralized Cloud: Impact of Communication Latency on the Energy Consumption of LTE Terminal Nodes. *Comput. Commun.* **2022**, *194*, 213–225. https://doi.org/10.1016/j.comcom.2022.07.026.

(10) Christensen, D. V.; Dittmann, R.; Linares-Barranco, B.; Sebastian, A.; Gallo, M. L.; Redaelli, A.; Slesazeck, S.; Mikolajick, T.; Spiga, S.; Menzel, S.; Valov, I.; Milano, G.; Ricciardi, C.; Liang, S.-J.; Miao, F.; Lanza, M.; Quill, T. J.; Keene, S. T.; Salleo, A.; Grollier, J.; Marković, D.; Mizrahi, A.; Yao, P.; Yang, J. J.; Indiveri, G.; Strachan, J. P.; Datta, S.; Vianello, E.; Valentian, A.; Feldmann, J.; Li, X.; Pernice, W. H. P.; Bhaskaran, H.; Furber, S.; Neftci, E.; Scherr, F.; Maass, W.; Ramaswamy, S.; Tapson, J.; Panda, P.; Kim, Y.; Tanaka, G.; Thorpe, S.; Bartolozzi, C.; Cleland, T. A.; Posch, C.; Liu, S.; Panuccio, G.; Mahmud, M.; Mazumder, A. N.; Hosseini, M.; Mohsenin, T.; Donati, E.; Tolu, S.; Galeazzi, R.; Christensen, M. E.; Holm, S.; Ielmini, D.; Pryds, N. 2022 Roadmap on Neuromorphic Computing and Engineering. *Neuromorphic Comput. Eng.* **2022**, *2* (2), 022501. https://doi.org/10.1088/2634-4386/ac4a83.

(11) Waser, R.; Dittmann, R.; Staikov, G.; Szot, K. Redox-Based Resistive Switching Memories – Nanoionic Mechanisms, Prospects, and Challenges. *Adv. Mater.* **2009**, *21* (25–26), 2632–2663. https://doi.org/10.1002/adma.200900375.

(12) Ding, G.; Zhao, J.; Zhou, K.; Zheng, Q.; Han, S.-T.; Peng, X.; Zhou, Y. Porous Crystalline Materials for Memories and Neuromorphic Computing Systems. *Chem. Soc. Rev.* **2023**, *52* (20), 7071–7136. https://doi.org/10.1039/D3CS00259D.

(13) Fatima, S.; Bin, X.; Mohammad, M. A.; Akinwande, D.; Rizwan, S. Graphene and MXene Based Free-Standing Carbon Memristors for Flexible 2D Memory Applications. *Adv. Electron. Mater.* **2022**, *8* (1), 2100549. https://doi.org/10.1002/aelm.202100549.

(14) Zhou, K.; Jia, Z.; Ma, X.-Q.; Niu, W.; Zhou, Y.; Huang, N.; Ding, G.; Yan, Y.; Han, S.-T.; Roy, V. A. L.; Zhou, Y. Manufacturing of Graphene Based Synaptic Devices for Optoelectronic Applications. *Int. J. Extreme Manuf.* **2023**, *5* (4), 042006. https://doi.org/10.1088/2631-7990/acee2e.

(15) Sun, L.; Zhang, Y.; Han, G.; Hwang, G.; Jiang, J.; Joo, B.; Watanabe, K.; Taniguchi, T.; Kim, Y.-M.; Yu, W. J.; Kong, B.-S.; Zhao, R.; Yang, H. Self-Selective van Der Waals Heterostructures for Large Scale Memory Array. *Nat. Commun.* **2019**, *10* (1), 3161. https://doi.org/10.1038/s41467-019-11187-9.

(16) Carta, D.; Salaoru, I.; Khiat, A.; Regoutz, A.; Mitterbauer, C.; Harrison, N. M.; Prodromakis, T. Investigation of the Switching Mechanism in TiO2-Based RRAM: A Two-Dimensional EDX Approach. *ACS Appl. Mater. Interfaces* **2016**, *8* (30), 19605–19611. https://doi.org/10.1021/acsami.6b04919.

(17) Hansen, M.; Ziegler, M.; Kolberg, L.; Soni, R.; Dirkmann, S.; Mussenbrock, T.; Kohlstedt, H. A Double Barrier Memristive Device. *Sci. Rep.* **2015**, *5* (1), 13753. https://doi.org/10.1038/srep13753.

(18) Hellenbrand, M.; Bakhit, B.; Dou, H.; Xiao, M.; Hill, M. O.; Sun, Z.; Mehonic, A.; Chen, A.; Jia, Q.; Wang, H.; MacManus-Driscoll, J. L. Thin Film Design of Amorphous Hafnium Oxide Nanocomposites Enabling Strong Interfacial Resistive Switching Uniformity. *Sci. Adv.* **2023**, *9* (25), eadg1946. https://doi.org/10.1126/sciadv.adg1946.

(19) Choi, S.; Kim, Y.; Van Nguyen, T.; Jeong, W. H.; Min, K.-S.; Choi, B. J. Low-Power Self-Rectifying Memristive Artificial Neural Network for Near Internet-of-Things Sensor Computing. *Adv. Electron. Mater.* **2021**, *7* (6), 2100050. https://doi.org/10.1002/aelm.202100050.

(20) Rana, A. M.; Akbar, T.; Ismail, M.; Ahmad, E.; Hussain, F.; Talib, I.; Imran, M.; Mehmood, K.; Iqbal, K.; Nadeem, M. Y. Endurance and Cycle-to-Cycle Uniformity Improvement in Tri-Layered CeO2/Ti/CeO2 Resistive Switching Devices by Changing Top Electrode Material. *Sci. Rep.* **2017**, *7* (1), 39539. https://doi.org/10.1038/srep39539.

(21) Ryu, J.-H.; Hussain, F.; Mahata, C.; Ismail, M.; Abbas, Y.; Kim, M.-H.; Choi, C.; Park, B.-G.; Kim, S. Filamentary and Interface Switching of CMOS-Compatible Ta2O5 Memristor for Non-Volatile Memory and Synaptic Devices. *Appl. Surf. Sci.* **2020**, *529*, 147167. https://doi.org/10.1016/j.apsusc.2020.147167.

(22) Lee, J.; Nikam, R. D.; Kwak, M.; Kwak, H.; Kim, S.; Hwang, H. Improvement of Synaptic Properties in Oxygen-Based Synaptic Transistors Due to the Accelerated Ion Migration in Sub-Stoichiometric Channels. *Adv. Electron. Mater.* **2021**, *7* (8), 2100219. https://doi.org/10.1002/aelm.202100219.

(23) Yao, X.; Klyukin, K.; Lu, W.; Onen, M.; Ryu, S.; Kim, D.; Emond, N.; Waluyo, I.; Hunt, A.; del Alamo, J. A.; Li, J.; Yildiz, B. Protonic Solid-State Electrochemical Synapse for Physical Neural Networks. *Nat. Commun.* **2020**, *11* (1), 3134. https://doi.org/10.1038/s41467-020-16866-6.

(24) Liu, Q.; Liu, Y.; Li, J.; Lau, C.; Wu, F.; Zhang, A.; Li, Z.; Chen, M.; Fu, H.; Draper, J.; Cao, X.; Zhou, C. Fully Printed All-Solid-State Organic Flexible Artificial Synapse for Neuromorphic Computing. *ACS Appl. Mater. Interfaces* **2019**, *11* (18), 16749–16757. https://doi.org/10.1021/acsami.9b00226.

(25) van de Burgt, Y.; Lubberman, E.; Fuller, E. J.; Keene, S. T.; Faria, G. C.; Agarwal, S.; Marinella, M. J.; Alec Talin, A.; Salleo, A. A Non-Volatile Organic Electrochemical Device as a Low-Voltage Artificial Synapse for Neuromorphic Computing. *Nat. Mater.* **2017**, *16* (4), 414–418. https://doi.org/10.1038/nmat4856.

(26) Lee, C.; Lee, J.; Kim, M.; Woo, J.; Koo, S.-M.; Oh, J.-M.; Lee, D. Two-Terminal Structured Synaptic Device Using Ionic Electrochemical Reaction Mechanism for Neuromorphic System. *IEEE Electron Device Lett.* **2019**, *40* (4), 546–549. https://doi.org/10.1109/LED.2019.2897777.

(27) Fuller, E. J.; Gabaly, F. E.; Léonard, F.; Agarwal, S.; Plimpton, S. J.; Jacobs-Gedrim, R. B.; James, C. D.; Marinella, M. J.; Talin, A. A. Li-Ion Synaptic Transistor for Low Power Analog Computing. *Adv. Mater.* **2017**, *29* (4), 1604310. https://doi.org/10.1002/adma.201604310.

(28) Kim, S.-E.; Lee, J.-G.; Ling, L.; Liu, S. E.; Lim, H.-K.; Sangwan, V. K.; Hersam, M. C.; Lee, H.-S. Sodium-Doped Titania Self-Rectifying Memristors for Crossbar Array Neuromorphic Architectures. *Adv. Mater.* **2022**, *34* (6), 2106913. https://doi.org/10.1002/adma.202106913.

(29) Lee, K.; Lee, J.; Nikam, R. D.; Heo, S.; Hwang, H. Sodium-Based Nano-Ionic Synaptic Transistor with Improved Retention Characteristics. *Nanotechnology* **2020**, *31* (45), 455204. https://doi.org/10.1088/1361-6528/abaa0e.

(30) Hodgkin, A. L.; Katz, B. The Effect of Sodium Ions on the Electrical Activity of the Giant Axon of the Squid - PMC. *J Physiol.* **1949**, *108* (1), 37–77. https://doi.org/10.1113/jphysiol.1949.sp004310.

(31) Arakaki, X.; Foster, H.; Su, L.; Do, H.; Wain, A. J.; Fonteh, A. N.; Zhou, F.; Harrington, M. G. Extracellular Sodium Modulates the Excitability of Cultured Hippocampal Pyramidal Cells. *Brain Res.* **2011**, *1401*, 85–94. https://doi.org/10.1016/j.brainres.2011.05.037.

(32) Halnes, G.; Mäki-Marttunen, T.; Keller, D.; Pettersen, K. H.; Andreassen, O. A.; Einevoll, G. T. Effect of Ionic Diffusion on Extracellular Potentials in Neural Tissue. *PLOS Comput. Biol.* **2016**, *12* (11), e1005193. https://doi.org/10.1371/journal.pcbi.1005193.

(33) Sun, F.; Lu, Q.; Feng, S.; Zhang, T. Flexible Artificial Sensory Systems Based on Neuromorphic Devices. *ACS Nano* **2021**, *15* (3), 3875–3899. https://doi.org/10.1021/acsnano.0c10049.

(34) Li, Y.; Lu, J.; Shang, D.; Liu, Q.; Wu, S.; Wu, Z.; Zhang, X.; Yang, J.; Wang, Z.; Lv, H.; Liu, M. Oxide-Based Electrolyte-Gated Transistors for Spatiotemporal Information Processing. *Adv. Mater.* **2020**, *32* (47), 2003018. https://doi.org/10.1002/adma.202003018.

(35) Pei, Y.; Yan, L.; Wu, Z.; Lu, J.; Zhao, J.; Chen, J.; Liu, Q.; Yan, X. Artificial Visual Perception Nervous System Based on Low-Dimensional Material Photoelectric Memristors. *ACS Nano* **2021**, *15* (11), 17319–17326. https://doi.org/10.1021/acsnano.1c04676.

(36) Wang, Y.; Cao, M.; Bian, J.; Li, Q.; Su, J. Flexible ZnO Nanosheet-Based Artificial Synapses Prepared by Low-Temperature Process for High Recognition Accuracy Neuromorphic Computing. *Adv. Funct. Mater.* **2022**, *32* (52), 2209907. https://doi.org/10.1002/adfm.202209907.

(37) Covi, E.; Donati, E.; Liang, X.; Kappel, D.; Heidari, H.; Payvand, M.; Wang, W. Adaptive Extreme Edge Computing for Wearable Devices. *Front. Neurosci.* **2021**, *15*. https://doi.org/10.3389/fnins.2021.611300.

(38) Fu, T.; Liu, X.; Fu, S.; Woodard, T.; Gao, H.; Lovley, D. R.; Yao, J. Self-Sustained Green Neuromorphic Interfaces. *Nat. Commun.* **2021**, *12* (1), 3351. https://doi.org/10.1038/s41467-021-23744-2.

(39) Sarkar, T.; Lieberth, K.; Pavlou, A.; Frank, T.; Mailaender, V.; McCulloch, I.; Blom, P. W. M.; Torricelli, F.; Gkoupidenis, P. An Organic Artificial Spiking Neuron for in Situ Neuromorphic Sensing and Biointerfacing. *Nat. Electron.* **2022**, *5* (11), 774–783. https://doi.org/10.1038/s41928-022-00859-y.

(40) Chen, D.; Wang, J.-H.; Chou, T.-F.; Zhao, B.; El-Sayed, M. A.; Liu, M. Unraveling the Nature of Anomalously Fast Energy Storage in T-Nb2O5. *J. Am. Chem. Soc.* **2017**, *139* (20), 7071–7081. https://doi.org/10.1021/jacs.7b03141.

(41) Griffith, K. J.; Forse, A. C.; Griffin, J. M.; Grey, C. P. High-Rate Intercalation without Nanostructuring in Metastable Nb2O5 Bronze Phases. *J. Am. Chem. Soc.* **2016**, *138* (28), 8888–8899. https://doi.org/10.1021/jacs.6b04345.

(42) Li, N.; Lan, X.; Wang, L.; Jiang, Y.; Guo, S.; Li, Y.; Hu, X. Precisely Tunable T-Nb2O5 Nanotubes via Atomic Layer Deposition for Fast-Charging Lithium-Ion Batteries. *ACS Appl. Mater. Interfaces* **2021**, *13* (14), 16445–16453. https://doi.org/10.1021/acsami.1c02207.

(43) Liu, Z.; Dong, W.; Wang, J.; Dong, C.; Lin, Y.; Chen, I.-W.; Huang, F. Orthorhombic Nb2O5-x for Durable High-Rate Anode of Li-Ion Batteries. *iScience* **2020**, *23* (1), 100767. https://doi.org/10.1016/j.isci.2019.100767.

(44) Deng, Q.; Yao, L. Advanced Nb2O5 Anode towards Fast Pseudocapacitive Sodium Storage. *Coatings* **2022**, *12* (12), 1873. https://doi.org/10.3390/coatings12121873.

(45) Liu, F.; Cheng, X.; Xu, R.; Wu, Y.; Jiang, Y.; Yu, Y. Binding Sulfur-Doped Nb2O5 Hollow Nanospheres on Sulfur-Doped Graphene Networks for Highly Reversible Sodium

Storage. *Adv. Funct. Mater.* **2018**, *28* (18), 1800394. https://doi.org/10.1002/adfm.201800394.

(46) Xu, J.; Wang, H.; Zhu, Y.; Liu, Y.; Zou, Z.; Li, G.; Xiong, R. Tunable Digital-to-Analog Switching in Nb2O5-Based Resistance Switching Devices by Oxygen Vacancy Engineering. *Appl. Surf. Sci.* **2022**, *579*, 152114. https://doi.org/10.1016/j.apsusc.2021.152114.

(47) Sahoo, S. Conduction and Switching Behavior of E-Beam Deposited Polycrystalline Nb2O5 Based Nano-Ionic Memristor for Non-Volatile Memory Applications. *J. Alloys Compd.* **2021**, *866*, 158394. https://doi.org/10.1016/j.jallcom.2020.158394.

(48) Zhou, Z.; Yang, M.; Fu, Z.; Wang, H.; Ma, X.; Gao, H. Electrode-Induced Polarity Conversion in Nb2O5/NbOx Resistive Switching Devices. *Appl. Phys. Lett.* **2020**, *117* (24), 243502. https://doi.org/10.1063/5.0020501.

(49) Deswal, S.; Jain, A.; Borkar, H.; Kumar, A.; Kumar, A. Conduction and Switching Mechanism in Nb2O5 Thin Films Based Resistive Switches. *Europhys. Lett.* **2016**, *116* (1), 17003. https://doi.org/10.1209/0295-5075/116/17003.

(50) Wylezich, H.; Mähne, H.; Rensberg, J.; Ronning, C.; Zahn, P.; Slesazeck, S.; Mikolajick, T. Local Ion Irradiation-Induced Resistive Threshold and Memory Switching in Nb2O5/NbOx Films. *ACS Appl. Mater. Interfaces* **2014**, *6* (20), 17474–17480. https://doi.org/10.1021/am5021149.

(51) Mähne, H.; Berger, L.; Martin, D.; Klemm, V.; Slesazeck, S.; Jakschik, S.; Rafaja, D.; Mikolajick, T. Filamentary Resistive Switching in Amorphous and Polycrystalline Nb2O5 Thin Films. *Solid-State Electron.* **2012**, *72*, 73–77. https://doi.org/10.1016/j.sse.2012.01.005.

(52) Nandi, S. K.; Nath, S. K.; Das, S. K.; Murdoch, B. J.; Ratcliff, T.; McCulloch, D. G.; Elliman, R. G. Effect of Interdiffusion and Crystallization on Threshold Switching Characteristics of Nb/Nb2O5/Pt Memristors. *ACS Appl. Mater. Interfaces* **2023**, *15* (50), 58613–58622. https://doi.org/10.1021/acsami.3c14431.

(53) Nath, S. K.; Nandi, S. K.; Ratcliff, T.; Elliman, R. G. Engineering the Threshold Switching Response of Nb2O5-Based Memristors by Ti Doping. *ACS Appl. Mater. Interfaces* **2021**, *13* (2), 2845–2852. https://doi.org/10.1021/acsami.0c19544.

(54) Nath, S. K.; Nandi, S. K.; Li, S.; Elliman, R. G. Metal-Oxide Interface Reactions and Their Effect on Integrated Resistive/Threshold Switching in NbOx. *Nanotechnology* **2020**, *31* (23), 235701. https://doi.org/10.1088/1361-6528/ab7889.

(55) Pan, X.; Shuai, Y.; Wu, C.; Luo, W.; Sun, X.; Zeng, H.; Zhou, S.; Böttger, R.; Ou, X.; Mikolajick, T.; Zhang, W.; Schmidt, H. Rectifying Filamentary Resistive Switching in Ion-Exfoliated LiNbO3 Thin Films. *Appl. Phys. Lett.* **2016**, *108* (3), 032904. https://doi.org/10.1063/1.4940372.

(56) Zaman, A.; Yakopcic, C.; Wang, S.; Shin, E.; Wang, W.; Taha, T. M.; Subramanyam, G. Analysis of Lithium Niobate Memristor Devices for Neuromorphic Programability. In *2019 IEEE National Aerospace and Electronics Conference (NAECON)*; 2019; pp 41–45. https://doi.org/10.1109/NAECON46414.2019.9058020.

(57) Wang, J.; Pan, X.; Wang, Q.; Luo, W.; Shuai, Y.; Xie, Q.; Zeng, H.; Niu, G.; Wu, C.; Zhang, W. Reliable Resistive Switching and Synaptic Plasticity in Ar+-Irradiated Single-Crystalline LiNbO3 Memristor. *Appl. Surf. Sci.* **2022**, *596*, 153653. https://doi.org/10.1016/j.apsusc.2022.153653.

(58) Han, H.; Jacquet, Q.; Jiang, Z.; Sayed, F. N.; Jeon, J.-C.; Sharma, A.; Schankler, A. M.; Kakekhani, A.; Meyerheim, H. L.; Park, J.; Nam, S. Y.; Griffith, K. J.; Simonelli, L.; Rappe, A. M.; Grey, C. P.; Parkin, S. S. P. Li Iontronics in Single-Crystalline T-Nb2O5 Thin Films with Vertical Ionic Transport Channels. *Nat. Mater.* **2023**, *22* (9), 1128–1135. https://doi.org/10.1038/s41563-023-01612-2.

(59) Ghosh, A.; Weidenbach, A. S.; Zivasatienraj, B.; McCrone, T. M.; Doolittle, W. A. Ion Intercalation Enabled Tunable Frequency Response in Lithium Niobite Memristors. *IEEE Trans. Electron Devices* **2023**, *70* (2), 776–781. https://doi.org/10.1109/TED.2022.3227498.

(60) Fan, Y.; Zhou, Z.; Liang, R.; Zhou, M.; Dong, X. The Effect of A-Site Nonstoichiometry on the Microstructure, Electric Properties, and Phase Stability of NaNbO3 Polycrystalline Ceramics. *J. Eur. Ceram. Soc.* **2019**, *39* (15), 4712–4718. https://doi.org/10.1016/j.jeurceramsoc.2019.06.041.

(61) Armstrong, C. L.; Price, M. B.; Muñoz-Rojas, D.; Davis, N. J. K. L.; Abdi-Jalebi, M.; Friend, R. H.; Greenham, N. C.; MacManus-Driscoll, J. L.; Böhm, M. L.; Musselman, K. P. Influence of an Inorganic Interlayer on Exciton Separation in Hybrid Solar Cells. *ACS Nano* **2015**, *9* (12), 11863–11871. https://doi.org/10.1021/acsnano.5b05934.

(62) Dong, H.; Yu, S.; Song, L.; Wang, X.; Wu, C. Fabrication of High-Quality Flexible Transparent Conductive Thin Films with a Nb2O5/AgNWs/Nb2O5 Sandwich Structure. *Ceram. Int.* **2022**, *48* (11), 15348–15354. https://doi.org/10.1016/j.ceramint.2022.02.068.

(63) Ouendi, S.; Arico, C.; Blanchard, F.; Codron, J.-L.; Wallart, X.; Taberna, P. L.; Roussel, P.; Clavier, L.; Simon, P.; Lethien, C. Synthesis of T-Nb2O5 Thin-Films Deposited by Atomic Layer Deposition for Miniaturized Electrochemical Energy Storage Devices. *Energy Storage Mater.* **2019**, *16*, 581–588. https://doi.org/10.1016/j.ensm.2018.08.022.

(64) Jan, A.; Rembert, T.; Taper, S.; Symonowicz, J.; Strkalj, N.; Moon, T.; Lee, Y. S.; Bae, H.; Lee, H. J.; Choe, D.-H.; Heo, J.; MacManus-Driscoll, J.; Monserrat, B.; Di Martino, G. In Operando Optical Tracking of Oxygen Vacancy Migration and Phase Change in Few Nanometers Ferroelectric HZO Memories. *Adv. Funct. Mater.* **2023**, *33* (22), 2214970. https://doi.org/10.1002/adfm.202214970.

(65) Kato, K.; Tamura, S. Die Kristallstruktur von T-Nb2O5. *Acta Crystallogr. B* **1975**, *31* (3), 673–677. https://doi.org/10.1107/S0567740875003603.

(66) Zidan, M. A.; Strachan, J. P.; Lu, W. D. The Future of Electronics Based on Memristive Systems. *Nat. Electron.* **2018**, *1* (1), 22–29. https://doi.org/10.1038/s41928-017-0006-8.

(67) Zhao, M.; Gao, B.; Tang, J.; Qian, H.; Wu, H. Reliability of Analog Resistive Switching Memory for Neuromorphic Computing. *Appl. Phys. Rev.* **2020**, *7* (1), 011301. https://doi.org/10.1063/1.5124915.

(68) Zeng, M.; He, Y.; Zhang, C.; Wan, Q. Neuromorphic Devices for Bionic Sensing and Perception. *Front. Neurosci.* **2021**, *15*. https://doi.org/10.3389/fnins.2021.690950.

(69) Gokmen, T.; Vlasov, Y. Acceleration of Deep Neural Network Training with Resistive Cross-Point Devices: Design Considerations. *Front. Neurosci.* **2016**, *10*. https://doi.org/10.3389/fnins.2016.00333.

(70) Mehonic, A.; Joksas, D.; Ng, W. H.; Buckwell, M.; Kenyon, A. J. Simulation of Inference Accuracy Using Realistic RRAM Devices. *Front. Neurosci.* **2019**, *13*. https://doi.org/10.3389/fnins.2019.00593.

(71) Mähne, H.; Wylezich, H.; Hanzig, F.; Slesazeck, S.; Rafaja, D.; Mikolajick, T. Analog Resistive Switching Behavior of Al/Nb2O5/Al Device. *Semicond. Sci. Technol.* **2014**, *29* (10), 104002. https://doi.org/10.1088/0268-1242/29/10/104002.

(72) Jin, H.; Jin, Q.; Jian, J.; Jin, H.; Jin, Q.; Jian, J. Smart Materials for Wearable Healthcare Devices. In *Wearable Technologies*; IntechOpen, 2018. https://doi.org/10.5772/intechopen.76604.

(73) Chen, H.; Li, H.; Ma, T.; Han, S.; Zhao, Q. Biological Function Simulation in Neuromorphic Devices: From Synapse and Neuron to Behavior. *Sci Technol Adv Mater* **2024**, *24* (1), 2183712. https://doi.org/10.1080%2F14686996.2023.2183712.

(74) Majumdar, S.; Tan, H.; Qin, Q. H.; van Dijken, S. Energy-Efficient Organic Ferroelectric Tunnel Junction Memristors for Neuromorphic Computing. *Adv. Electron. Mater.* **2019**, *5* (3), 1800795. https://doi.org/10.1002/aelm.201800795.

(75) Kumar, S.; Williams, R. S.; Wang, Z. Third-Order Nanocircuit Elements for Neuromorphic Engineering. *Nature* **2020**, *585* (7826), 518–523. https://doi.org/10.1038/s41586-020-2735-5.

(76) Kumar, S.; Wang, X.; Strachan, J. P.; Yang, Y.; Lu, W. D. Dynamical Memristors for Higher-Complexity Neuromorphic Computing. *Nat. Rev. Mater.* **2022**, *7* (7), 575–591. https://doi.org/10.1038/s41578-022-00434-z.

(77) Li, M.; Hong, Q.; Wang, X. Memristor-Based Circuit Implementation of Competitive Neural Network Based on Online Unsupervised Hebbian Learning Rule for Pattern Recognition. *Neural Comput. Appl.* **2022**, *34* (1), 319–331. https://doi.org/10.1007/s00521-021-06361-4.

(78) Kim, K.-N.; Sung, M.-J.; Park, H.-L.; Lee, T.-W. Organic Synaptic Transistors for Bio-Hybrid Neuromorphic Electronics. *Adv. Electron. Mater.* **2022**, *8* (1), 2100935. https://doi.org/10.1002/aelm.202100935.

(79) Levy, W. B.; Steward, O. Temporal Contiguity Requirements for Long-Term Associative Potentiation/Depression in the Hippocampus. *Neuroscience* **1983**, *8* (4), 791–797. https://doi.org/10.1016/0306-4522(83)90010-6.

(80) Jan, A.; Strkalj, N.; Nguyen, X. T.; MacManus-Driscoll, J. L.; Martino, G. D. Comprehensive Study of Raman Optical Response of Typical Substrates for Thin-Film Growth under 633 Nm and 785 Nm Laser Excitation. *Opt. Express* **2023**, *31* (21), 33914–33922. https://doi.org/10.1364/OE.504002.

(81) Orel, B.; Maček, M.; Grdadolnik, J.; Meden, A. In Situ UV-Vis and Ex Situ IR Spectroelectrochemical Investigations of Amorphous and Crystalline Electrochromic Nb2O5 Films in Charged/Discharged States. *J. Solid State Electrochem.* **1998**, *2* (4), 221–236. https://doi.org/10.1007/s100080050092.

(82) Jehng, J. M.; Wachs, I. E. Structural Chemistry and Raman Spectra of Niobium Oxides. *Chem. Mater.* **1991**, *3* (1), 100–107. https://doi.org/10.1021/cm00013a025.

(83) Hellenbrand, M.; MacManus-Driscoll, J. Multi-Level Resistive Switching in Hafnium-Oxide-Based Devices for Neuromorphic Computing. *Nano Converg.* **2023**, *10* (1), 44. https://doi.org/10.1186/s40580-023-00392-4.

(84) Zhang, S.; Liu, G.; Qiao, W.; Wang, J.; Ling, L. Oxygen Vacancies Enhance the Lithium Ion Intercalation Pseudocapacitive Properties of Orthorhombic Niobium Pentoxide. *J. Colloid Interface Sci.* **2020**, *562*, 193–203. https://doi.org/10.1016/j.jcis.2019.12.015.

(85) Zheng, Y.; Yao, Z.; Shadike, Z.; Lei, M.; Liu, J.; Li, C. Defect-Concentration-Mediated T-Nb2O5 Anodes for Durable and Fast-Charging Li-Ion Batteries. *Adv. Funct. Mater.* **2022**, *32* (12), 2107060. https://doi.org/10.1002/adfm.202107060.

(86) Wang, S. L.; Xue, Y.; Sun, H. Electrochemical Study on the Electrodeoxidation of Nb2O5 in Equimolar CaCl2 and NaCl Melt. *J. Electroanal. Chem.* **2006**, *595* (2), 109–114. https://doi.org/10.1016/j.jelechem.2006.07.013.

(87) Kumagai, N.; Satodate, K.; Tanno, K. Kinetics of Electrochemical Lithium Intercalation into Nb2O5 as an Electrode Material for Secondary Lithium Batteries. *Electrochem Soc Japan* **1994**, *62* (1), 56–64.

(88) Slade, R. C. T.; Barker, J.; Halstead, T. K. Protonic Conduction and Diffusion in the Hydrous Oxides V2O5·*n*H2O, Nb2O5·*n*H2O, Ta2O5·*n*H2O and CeO2·*n*H2O. *Solid State Ion.* **1987**, *24* (2), 147–153. https://doi.org/10.1016/0167-2738(87)90023-3.

(89) Chen, W. K.; Jackson, R. A. Diffusion of Oxygen in Near-Stoichiometric α-Nb2O5. *J. Chem. Phys.* **1967**, *47* (3), 1144–1148. https://doi.org/10.1063/1.1711999.

(90) Chen, W. K.; Swalin, R. A. Studies on the Defect Structure of α-Nb2O5. *J. Phys. Chem. Solids* **1966**, *27* (1), 57–64. https://doi.org/10.1016/0022-3697(66)90164-8.

(91) Nakamura, R.; Toda, T.; Tsukui, S.; Tane, M.; Ishimaru, M.; Suzuki, T.; Nakajima, H. Diffusion of Oxygen in Amorphous Al2O3, Ta2O5, and Nb2O5. *J. Appl. Phys.* **2014**, *116* (3), 033504. https://doi.org/10.1063/1.4889800.